Engineered signaling centers for the spatially controlled patterning of human pluripotent stem cells

Andrea Manfrin[1], Yoji Tabata[1], Eric R. Paquet[2], Ambroise R. Vuaridel[2], François R. Rivest[1], Felix Naef[2], Matthias P. Lutolf[1,3,*]

[1]Laboratory of Stem Cell Bioengineering, Institute of Bioengineering (IBI), School of Life Sciences (SV) and School of Engineering (STI), École Polytechnique Fédérale de Lausanne (EPFL), 1015 Lausanne, Switzerland.

[2]Computational Systems Biology Lab, IBI, SV, EPFL, 1015 Lausanne, Switzerland.

[3]Institute of Chemical Sciences and Engineering, School of Basic Science (BS), EPFL, 1015 Lausanne, Switzerland.

*To whom correspondence should be addressed. Email: matthias.lutolf@epfl.ch

Editorial Summary (250 characters max.):

A microfluidic approach allows spatiotemporal control over morphogen distribution in human pluripotent stem cell cultures. This approach recapitulates early developmental processes such as localized signaling and symmetry breaking events.

Signaling centers, localized groups of cells that secrete morphogens, play a key role in early development and organogenesis by orchestrating spatial cell fate patterning. Here we present a microfluidic approach that exposes human pluripotent stem cell (hPSC) colonies to spatiotemporally controlled morphogen gradients generated from artificial signaling centers. In response to a localized source of BMP4, hPSC colonies reproducibly break their intrinsic radial symmetry to produce distinct, axially arranged differentiation domains. Counteracting sources of the BMP antagonist NOGGIN enhance this spatial control of cell fate patterning. We also show how morphogen concentration and cell density impact the BMP response and germ-layer patterning.

These results demonstrate that the intrinsic capacity of stem cells for self-organization can be extrinsically controlled through the use of engineered signaling centers.

Introduction

Human pluripotent stem cells (hPSCs) are a powerful tool for studying human development and cell fate patterning[1–4]. Geometrically confined human embryonic stem cell (hESC) colonies uniformly exposed to morphogens such as BMP4, WNT3a, or Activin A generate radially symmetric patterns of different cell types[5–7]. These in vitro phenomena may reflect behaviors involved in pattern formation during early human development, particularly in gastrulation[3,5,6]. Specifically, exposing hESC colonies to BMP4 causes a concentric organization of cell types with trophoblast-like cells forming at the edge of the colony, an inner region of ectodermal cells, and primitive streak-like cells and their derivatives in between[5,6].

Despite the impressive multicellular self-organization, the radially symmetric spatial arrangement of cells observed in this embryonic organoid system does not reflect the physiological reality. Indeed, detailed molecular studies in animal models of development[8,9], as well as anatomical and histological analyses in primate embryos[10], suggest a more asymmetrical organization of these cell types along the future anterior-posterior axis of the early human embryo. As opposed to the uniform distribution of morphogens in vitro, the formation of these spatial patterns in vivo is guided by the presence of signaling centers, which are localized groups of cells that secrete morphogens and/or morphogen inhibitors in specific local concentrations to spatially and temporally shape the activity of signaling pathways in the targeted tissues[9,11]. Studies in mouse embryos have, for example, shown that a posteriorly localized increase of BMP4 activity plays an important role in primitive streak emergence and regionalization, contributing to the specification of its most posterior derivatives[9].

Even though localized morphogen signaling is important in vivo, existing hPSC culture systems do not provide the ability to explore localized morphogen signaling. In such systems, an experimenter has little control over self-organization beyond providing signaling molecules at a given concentration as media supplements to the entire culture system (i.e., in bulk). To overcome this problem, we herein report a microfluidic approach for emulating signaling centers in stem cell culture. We engineered a microdevice to establish spatially oriented and dynamic concentration gradients. We exposed geometrically confined hESC colonies to gradients of BMP4, with the aim of breaking the intrinsic radial symmetry of the system towards an in vivo-like axial germ layer arrangement. We show how an asymmetric signaling environment is interpreted by hESCs in terms of signaling pathway activity and how various extrinsic parameters (BMP4 concentration at the source, initial cell density and colony size) affect cell fate patterning. Finally, to increase the spatial control over the patterning process, we exposed hESC colonies to counteracting gradients of a morphogen and its inhibitor, which

even more closely emulated cell fate patterning environments during early embryonic development in vivo.

Results

A microfluidic device for exposing hPSCs to localized morphogen sources

To expose hPSC colonies to spatially and temporally controlled signaling gradients emanating from a localized source, we developed a poly(dimethylsiloxane) (PDMS)-based microfluidic cell culture device (**Fig. 1a,b,c, Supplementary Fig. 1a,b,c**) whose dimensions were designed to allow for the self-organization of geometrically confined hESC colonies[5,6]. The device is composed of four parallel cell chambers, each separated from external perfusion channels by inert poly(ethylene glycol) (PEG) hydrogel[12] barriers (**Fig. 1a,b, Supplementary Fig. 1b**) which confine the cells, and generate, without unwanted convective flow[13], concentration gradients following a classical source-sink model of Fickian diffusion. Computational simulations and diffusion experiments with fluorescently labeled 40 kDa dextran demonstrated that our device indeed allows for the generation of time-evolving concentration gradients (**Fig. 1d,e,f,g**). The presence of phase-guiding features only minimally affects the concentration profile at each time point at the chamber edges (**Supplementary Fig. 1d,e**). Notably, by adapting the chip design shown in **Figure 1a** to comprise additional medium inlets, time-controllable pulsatile gradients can be readily generated (**Supplementary Fig. 1f,g,h**).

We next tested the suitability of our microsystem for the maintenance and germ-layer patterning of geometrically confined hESC colonies[5,6,14]. While perfused with maintenance medium, hESCs expand and retain the expression of the pluripotency markers OCT4 and SOX2 after 96 hours in the cell chamber (**Fig. 1h**). Uniform exposure of the colonies to 50 ng/mL of BMP4 results in an initially uniform phosphorylation of SMAD1 at serines 463 and 465 (pSMAD1) that becomes progressively restricted to the colony edges (**Fig. 1i**)[6,14]. After 48 hours of BMP4 exposure, radially symmetric domains of cell fates emerge: an ectodermal domain marked by nuclear SOX2 at the colony center (**Fig. 1j**) next to a primitive streak-like domain with cells positive for MIXL1 (labeled with GFP) and TBXT (T/Brachyury) (**Fig. 1j,k, Supplementary Fig. 2a**). In addition, a more peripheral layer of cells is positive for the posterior marker CDX2 (**Fig. 1j,k, Supplementary Fig. 2a,b,c**) and the endodermal marker SOX17 (**Fig. 1j,k, Supplementary Fig. 2a,c,d**), with some of the SOX17 cells co-expressing MIXL1 (**Supplementary Fig. 2d**). Most of the CDX2-positive cells are positive for SOX17 (**Supplementary Fig. 2c**) and some of them also for MIXL1 (**Supplementary Fig. 2b**), suggesting, based on recent data from an in vitro mouse gastrulation model[15], a posterior

extraembryonic mesodermal identity for these cells. Finally, at the edge of the colony, we occasionally observed patches of morphologically distinct CDX2-only positive cells previously described as trophoblast-like cells[5,16] with large nuclei and wider internuclear spaces (**Supplementary Fig. 2b,c,e**). Taken together, these data show that our device can be used to approximate the behavior of morphogens diffusing from signaling centers and is compatible with the maintenance and spatial cell fate patterning (**Supplementary Fig. 2f**) of geometrically confined hESC colonies.

Differentiation of hESC in response to a localized morphogen source

We postulated that the presence of a microfluidically generated BMP4 gradient should result in asymmetrical activity of the BMP pathway in hESC colonies, potentially translating into an asymmetrical pattern of cell fates. To predict BMP pathway activity triggered by BMP4 stimulation, we employed a two-dimensional version of a recently published in silico model[14]. The uniform exposure to 50 ng/ml of BMP4 matches the previously reported radially symmetric restriction of BMP activity to the colony edges[14] (**Supplementary Fig. 2g**), whereas this model indeed predicts an asymmetrical BMP activity for a localized morphogen source (**Fig. 2a, Supplementary Fig. 3a**).

Measurements of pSMAD1 dynamics in response to BMP4 gradients (50 ng/ml at the source) agree with the in silico prediction (**Fig. 2b**), especially for the initial time points. However, we observed that after ~12 hours of graded BMP4 stimulation, pSMAD1 becomes almost exclusively restricted to the source side (**Fig. 2b,c**). This spatiotemporal asymmetry of BMP activity results in a highly asymmetrical allocation of cell fates: MIXL1 and T/Brachyury are mainly expressed on the BMP4 source side, with a much smaller domain of expression close to the sink (**Fig. 2d,e, Supplementary Fig. 3b,c,d**). We also identified a spatially asymmetrical expression pattern for nuclear SOX2 (**Fig. 2d**) and SOX17 (**Fig. 2d-f, Supplementary Fig. 3b-d**). Under graded BMP4 stimulation, the aforementioned putative posterior extraembryonic mesodermal cells, co-expressing SOX17 and CDX2, were almost exclusively found at the source side, which contrasts with the SOX17-positive CDX2-negative cells that were found at the sink side (**Fig. 2f**). These data show that the exposure of hESC colonies to graded BMP4 results in an axial arrangement of cell fates, with a more posterior cellular identity localized close to the BMP4 source. We note that the described behaviors appear to be highly stereotypical and apply to other hESC lines, such as H1 and RUES2 (**Supplementary Fig. 4a-c**). A hiPSC line (HYS0103) that we tested showed a clearly asymmetrical expression of CDX2 (**Supplementary Fig. 4d,e**), yet T/Brachyury was far less restricted, even at lower BMP4 concentrations. Finally, we also note that the patterning induced by a gradient of BMP4 does not scale with hESC colony size: on half-sized colonies (i.e. 500μm in diameter;

Supplementary Fig. 5a-c) we found the axial asymmetric arrangement of MIXL1 and CDX2 to be reduced (**Supplementary Fig. 5d,e**).

Modulation of morphogen source concentration shifts germ layer boundaries and affects differentiation dynamics

One of the defining properties of a morphogen is its capacity to drive concentration-dependent cell fate allocation. We reasoned that our system could be ideal for probing how modulating the morphogen gradient profile impacts patterning. A five-fold increase in BMP4 concentration at the source (250 ng/ml) resulted in much faster and more uniform pathway activation, with a longer timespan needed to restrict pSMAD1 towards the source (**Fig. 3a,b**). After 48 hours, the MIXL1, BRA, and SOX17 domains shifted from the source more towards the center of the colonies, and their domains at the sink expanded (**Fig. 3c,d, Supplementary Fig. 6a**). Moreover, at 50 ng/ml of BMP4 a CDX2 domain could only be detected close to the source (**Fig. 2d,f**), though at high morphogen concentrations, CDX2-positive cells also appeared near the sink (**Fig. 3c,d, Supplementary Fig. 6a**), suggesting an extension of the posterior identity to this region. Additionally, we identified a pronounced domain of large, flat CDX2-positive trophoblast-like cells on the source side at higher concentrations [5,16], which is rarely detectable at lower BMP4 concentrations (**Fig. 3c,d, Supplementary Fig. 6a,b**). Therefore, modulating the morphogen concentration at the source shifts the boundaries between different cell fates, demonstrating that our in vitro approach captures the concept of morphogen-driven positional information[17].

The differences observed in germ layer allocation upon different BMP4 source concentrations prompted us to focus on the differentiation dynamics at different conditions. We thus assessed how a BMP4 gradient at different source concentrations (10 ng/ml, 50 ng/ml and 250 ng/ml) influences the differentiation of HES3 MIXL1$^{GFP/+}$ cells towards the primitive streak lineage. We observed differences in the dynamics of MIXL1 domain emergence among the tested conditions (**Fig. 4a-c, Video 1-6**). Specifically, at 10 ng/ml of BMP4, MIXL1 took longer to be expressed, and MIXL1-positive cells were only apparent at the source side of the culture chamber (**Fig. 4a, Video 1,2**). At 50 ng/ml, MIXL1 was first expressed close to the BMP4 source then later appeared at the sink side (**Fig. 4b, Video 3,4**). At the highest BMP4 concentration (250 ng/ml), MIXL1 expression emerged from a region close to the center of the colony (**Fig. 4c, Video 5,6**), in line with what we found for other primitive streak (and derivatives) markers. Under these conditions, MIXL1 appeared simultaneously at the source and sink. Taken together, these experiments demonstrate that patterning dynamics are dependent on the morphogen concentration at the source.

Effect of cell density on germ-layer patterning

During embryonic development, morphogen-receiving cells can actively change the surrounding gradient through morphogen uptake and degradation, and cell density can also impact morphogen diffusion[18–20]. In silico modeling predicts a reduction in BMP activity at higher initial cell densities for colonies exposed to 50 ng/ml of BMP4 (**Supplementary Fig. 7a**). Thus, we conducted a series of experiments to test for this dependency on cell density. We loaded hESC suspensions into the culture chamber at three different concentrations (**Supplementary Fig. 7b,c**), resulting in cell monolayers of different densities – "low", "intermediate", and "high", with "intermediate" corresponding to the density used up to this point (**Supplementary Fig. 7b,c**). "High density" hESC colonies exposed to BMP4 resulted in MIXL1, SOX17, and CDX2 expression exclusively near the morphogen source (**Fig. 5a,b, Supplementary Fig. 7d**), with cells outside this domain expressing nuclear SOX2 (**Fig. 5a**). The phenotypic difference compared to "intermediate density" colonies (**Fig. 5b** and compare **Fig. 2d** with **Fig. 5a**) demonstrates that cell density alone can spatially restrict the effects of a localized source of BMP4. Exposing "high density" colonies to higher BMP4 source concentrations (150 ng/ml or higher) imposed the previously observed asymmetric phenotype, with MIXL1 positive cells at the sink side (**Fig. 5c,d, Supplementary Fig. 7e**) – results that are in accordance with in silico model predictions (**Supplementary Fig. 7f**). "Low density" colonies exposed to the standard BMP4 concentration (50 ng/ml) at the source did not show any noticeable germ-layer patterning, as evidenced by the almost ubiquitous expression of MIXL1 and CDX2 across the colony (**Supplementary Fig. 7g**). Therefore, a minimal initial cell density is required for the pattern to emerge in our system, as was previously shown in the classical system[14]. Collectively, these data show that cell density plays an important role in shaping the asymmetrical response of the colony to localized BMP4 stimulation, likely by affecting morphogen distribution. Our results also suggest that it may be the balance between cell density and morphogen quantity that determines the final patterning outcome in our system.

Effect of a counteracting morphogen-inhibitor pair on germ-layer patterning

During embryonic development, the effect of morphogens is often modulated by the presence of opposing gradients of related inhibitors, such as during anterior-posterior (AP) patterning of the epiblast in which the primitive streak emerges on the future posterior side[8,9,21]. We sought to replicate this logic in our system to test whether cell fate patterning could be directed to acquire a more in vivo-like AP axial organization. To this end, the BMP4 gradient was counteracted with an opposing source of NOGGIN, one of its diffusible inhibitors[22]. We found that NOGGIN indeed prevents the activation of the BMP pathway in cells close to the sink for all the time points tested (**Fig. 6a,b**). After 48 hours, these BMP pathway dynamics resulted

in the robust restriction of the MIXL1, T/Brachyury, SOX17, and CDX2 domains exclusively at the source side (**Fig. 6c,d, Supplementary Fig. 8a-c**). Nuclear SOX2 was present in cells all over the colony, with the exception of the regions closest to the source (**Fig. 6c**). We observed the restriction of T/Brachyury and CDX2 at the BMP4 side and the presence of nuclear SOX2 at the NOGGIN side for other hESC lines (H1, RUES2) (**Supplementary Fig. 9a-c**), for one hiPSC line (HYS0103) (**Supplementary Fig. 9d,e**) and for HES3 MIXL1$^{GFP/+}$ cells on half-sized colonies (**Supplementary Fig. 10a,b**). These experiments show that our approach is well suited for establishing counteracting morphogen-inhibitor gradients that provide additional control over hPSC germ-layer patterning.

Discussion

We introduce a versatile method for spatiotemporally controlling germ-layer patterning of hPSCs through exposure to artificial signaling centers. In our system, patterning is the result of a previously described intrinsic, radial, self-patterning process[5,6,14] driven extrinsically through morphogen gradients. Similar to in vivo signaling centers, the morphogen gradients in our device are established through diffusion and change over time. In our system as well, gradient profiles are likely also influenced by the presence of the cells themselves, an effect that is technically challenging to elucidate directly. Nonetheless, the dynamics of the BMP pathway activity served as a good proxy for the temporal evolution of the morphogen gradient in the presence of the cells.

In mouse embryos, BMP4 is involved in primitive streak emergence, and its sustained activity on the posterior cells is responsible for the formation of posterior derivatives, such as the CDX2-expressing extraembryonic mesoderm[9,15,23,24,25]. Primitive streak cells that migrate away from the BMP4 source are exposed to the morphogen for shorter periods of time and give rise to more anterior primitive streak derivatives[8,9,15]. Hence, the initially uniform activation of the BMP pathway and its progressive restriction to the BMP4 source in our system may mimic the signaling that underlies primitive streak emergence and patterning in vivo.

The BMP4 dose-dependent differences in the phenotype that we observed could be caused by differences in the length of BMP pathway activation experienced by a cell according to its position in the colony. However, this does not rule out the possibility that cells can also directly interpret BMP4 concentrations. Indeed, even though the BMP pathway is always active in cells at or close to the BMP4 source, at very high concentrations, a different phenotype was seen (i.e. the expansion of the trophoblast-like cell domain). Importantly, it should be noted that secondary signaling from other endogenously produced ligands such as NODAL or WNT3 very likely plays a role in determining the final patterning outcome[7,14].

We detected a cell density dependence for the response of the colonies to localized BMP4 sources. The in silico model that we used does not fully capture the spatial restriction of the BMP pathway activity at the source that we detected in experiments. This suggests that other cell–density-dependent mechanisms could be involved in shaping the dynamics of the pathway in our system. One possibility is that the morphogen gradient itself is reshaped by the increasing number of cells, an effect that has been proposed in vivo to be caused by cell-mediated morphogen uptake and degradation[18,26–28].

The spatial control of BMP4 activity in our system can be further refined by the use of the counteracting inhibitor NOGGIN. This condition allowed us to localize the artificial primitive streak and its derivatives to only one side of the colony in an arrangement resembling a physiologically posterior location of the primitive streak at the stage of its emergence from the epiblast[9,10].

Taken together, our microfluidic approach for engineering asymmetrical signaling environments allowed us to induce asymmetrical cell fate choices within individual hPSC colonies. Previously reported microfluidic approaches employed for stem cell patterning experiments either do not afford pronounced temporal asymmetry of signaling[13,29] or offer limited space for a graded distribution of signaling molecules[30]. Other technologies are based on the exposure of cells to convective flow, and as such, preclude the possibility of studying effects derived from the production of paracrine factors, limiting the study of self-organizing systems[31]. Importantly, whereas previous studies focused on loosely interacting cell populations[29,30,32,33], our approach is based on coherent colonies of epithelial-like cells in which cell-cell interactions may allow more elaborate self-organization. Our system should be broadly applicable for uncovering how gradients of morphogens operate in determining cell fate patterning, such as for exploring how temporal variations in the signaling environment influence cell fate choices in space. Ultimately, this approach may be useful for building more complex physiological signaling environments to quantitatively study symmetry breaking and cell fate patterning events or other complex cell behaviors that occur during early embryonic development and organogenesis.

ACKNOWLEDGMENTS

We thank Andrew G. Elefanty (The Royal Children Hospital) for providing the HES3 MIXL1$^{GFP/+}$ hESC line and Ali H. Brivanlou (The Rockefeller University) for providing the RUES2 hESC line. We thank Nathalie Brandenberg (EPFL) for help with diffusion studies and Omid Mashinchian (EPFL and Nestlé Institute of Health Sciences) for suggestions on HYS0103 hiPSC line culture. We thank Luciano Manfrin for helping with tools for the syringe pumps setup. We thank Giuliana Rossi and all the members of the Laboratory of Stem Cell Bioengineering (EPFL) for helpful discussions. A.M. is supported by the “EPFL Fellows” program co-funded by the Marie Skłodowska-Curie, Horizon2020 (Grant agreement 665667). E.R.P. was supported by a Canadian Institute of Health Research (CIHR 358808) and a SystemsX.ch Transition Postdoc Fellowship (51FSP0163584). A.R.V. and F.N. were supported by StoNets, a grant from the Swiss SystemsX.ch (www.systemsx.ch) initiative evaluated by the Swiss National Science Foundation. This work was funded by the EU

Framework7 HEALTH research programme Plurimes (http://plurimes.eu), the European Union's Horizon 2020 research and innovation programme (INTENS 668294), Swiss National Science Foundation (grant #310030_179447), the Personalized Health and Related Technologies Initiative from the ETH Board and École Polytechnique Fédérale de Lausanne (EPFL).

AUTHOR CONTRIBUTIONS

A.M. and M.P.L. conceived the study and designed the experiments; A.M. and Y.T. performed the experiments; Y.T. designed the original diffusion device; A.M., Y.T. and F.R.R. produced the PDMS microfluidic devices; M.P.L. and A.M. wrote the manuscript; E.R.P. performed the fluorescence intensity based image analysis; A.M. performed the percentage of marker-positive cell image analysis; A.R.V. and F.N. analyzed the mathematical model; all authors read and approved the final manuscript.

COMPETING FINANCIAL INTERESTS

The authors declare no competing financial interests.

References

1. McCauley, H. A. & Wells, J. M. Pluripotent stem cell-derived organoids: using principles of developmental biology to grow human tissues in a dish. *Development* **144**, 958–962 (2017).
2. Simunovic, M. & Brivanlou, A. H. Embryoids, organoids and gastruloids: new approaches to understanding embryogenesis. *Development* **144**, 976–985 (2017).
3. Taniguchi, K., Heemskerk, I. & Gumucio, D. L. Opening the black box: Stem cell–based modeling of human post-implantation development. *J. Cell Biol.* jcb.201810084 (2018). doi:10.1083/jcb.201810084
4. Rossi, G., Manfrin, A. & Lutolf, M. P. Progress and potential in organoid research. *Nat. Rev. Genet.* **19**, 671–687 (2018).
5. Warmflash, A., Sorre, B., Etoc, F., Siggia, E. D. & Brivanlou, A. H. A method to recapitulate early embryonic spatial patterning in human embryonic stem cells. *Nat. Methods* **11**, 847–854 (2014).
6. Tewary, M. *et al.* A stepwise model of reaction-diffusion and positional information governs self-organized human peri-gastrulation-like patterning. *Development* **144**, 4298–4312 (2017).
7. Martyn, I., Kanno, T. Y., Ruzo, A., Siggia, E. D. & Brivanlou, A. H. Self-organization of a human organizer by combined Wnt and Nodal signalling. *Nature* **558**, 132–135 (2018).
8. Tam, P. P. L. & Loebel, D. A. F. Gene function in mouse embryogenesis: get set for gastrulation. *Nat. Rev. Genet.* **8**, 368–381 (2007).
9. Arnold, S. J. & Robertson, E. J. Making a commitment: cell lineage allocation and axis patterning in the early mouse embryo. *Nat. Rev. Mol. Cell Biol.* **10**, 91–103 (2009).
10. Schoenwolf, G. C., Bleyl, S. B., Brauer, P. R. & Francis-West, P. H. *Larsen's Human Embriology*. (Elsevier/Churchill Livingstone, 2014).
11. Briscoe, J. & Small, S. Morphogen rules: design principles of gradient-mediated embryo patterning. *Development* **142**, 3996–4009 (2015).
12. Gobaa, S. *et al.* Artificial niche microarrays for probing single stem cell fate in high throughput. *Nat. Methods* **8**, 949–955 (2011).
13. Keenan, T. M. & Folch, A. Biomolecular gradients in cell culture systems. *Lab Chip* **8**, 34–57 (2008).
14. Etoc, F. *et al.* A Balance between Secreted Inhibitors and Edge Sensing Controls Gastruloid Self-Organization. *Dev. Cell* **39**, 302–315 (2016).
15. Morgani, S. M., Metzger, J. J., Nichols, J., Siggia, E. D. & Hadjantonakis, A.-K. Micropattern differentiation of mouse pluripotent stem cells recapitulates embryo regionalized cell fate patterning. *Elife* **7**, e32839 (2018).
16. Schulz, L. C. *et al.* Human Embryonic Stem Cells as Models for Trophoblast Differentiation. *Placenta* **29**, 10–16 (2008).
17. Wolpert, L. Positional Information and the Spatial Pattern of Cellular Differentiation. *J. Theor. Biol.* **25**, 1–47 (1969).
18. Rogers, K. W. & Schier, A. F. Morphogen Gradients: From Generation to Interpretation. *Annu. Rev. Cell Dev. Biol.* **27**, 377–407 (2011).
19. Kutejova, E., Briscoe, J. & Kicheva, A. Temporal dynamics of patterning by morphogen gradients. *Curr. Opin. Genet. Dev.* **19**, 315–322 (2009).
20. Muller, P., Rogers, K. W., Yu, S. R., Brand, M. & Schier, A. F. Morphogen transport. *Development* **140**, 1621–1638 (2013).
21. Piccolo, S., Sasai, Y., Bin, L. & De Robertis, E. M. Dorsoventral Patterning in Xenopus: Inhibition of Ventral Signals by Direct Binding of Chordin to BMP-4. *Cell* **86**, 589–598 (1996).
22. Zimmerman, L. B., De Jesus-Escobar, J. M. & Harland, R. M. The Spemann Organizer Signal noggin Binds and Inactivates Bone Morphogenetic Protein 4. *Cell* **86**, 599–606 (1996).

23. Winnier, G., Blessing, M., Labosky, P. A. & Hogan, B. L. M. Bone morphogenetic protein-4 Is required for mesoderm formation and patterning in the mouse. *Genes Dev.* **9**, 2105–2116 (1995).
24. Ben-Haim, N. *et al.* The Nodal Precursor Acting via Activin Receptors Induces Mesoderm by Maintaining a Source of Its Convertases and BMP4. *Dev. Cell* **11**, 313–323 (2006).
25. Bier, E. & De Robertis, E. M. BMP gradients: A paradigm for morphogen-mediated developmental patterning. *Science* **348**, aaa5838–aaa5838 (2015).
26. Schwank, G. *et al.* Formation of the Long Range Dpp Morphogen Gradient. *PLoS Biol.* **9**, e1001111 (2011).
27. Zhou, S. *et al.* Free Extracellular Diffusion Creates the Dpp Morphogen Gradient of the Drosophila Wing Disc. *Curr. Biol.* **22**, 668–675 (2012).
28. Yu, S. R. *et al.* Fgf8 morphogen gradient forms by a source-sink mechanism with freely diffusing molecules. *Nature* **461**, 533–536 (2009).
29. Demers, C. J. *et al.* Development-on-chip: *in vitro* neural tube patterning with a microfluidic device. *Development* **143**, 1884–1892 (2016).
30. Kawada, J., Kimura, H., Akutsu, H., Sakai, Y. & Fujii, T. Spatiotemporally controlled delivery of soluble factors for stem cell differentiation. *Lab. Chip* **12**, 4508 (2012).
31. Titmarsh, D. M. *et al.* Microbioreactor Arrays for Full Factorial Screening of Exogenous and Paracrine Factors in Human Embryonic Stem Cell Differentiation. *PLoS ONE* **7**, e52405 (2012).
32. Uzel, S. G. M. *et al.* Simultaneous or Sequential Orthogonal Gradient Formation in a 3D Cell Culture Microfluidic Platform. *Small* **12**, 612–622 (2016).
33. Tabata, Y. & Lutolf, M. P. Multiscale microenvironmental perturbation of pluripotent stem cell fate and self-organization. *Sci. Rep.* **7**, (2017).

Figures:

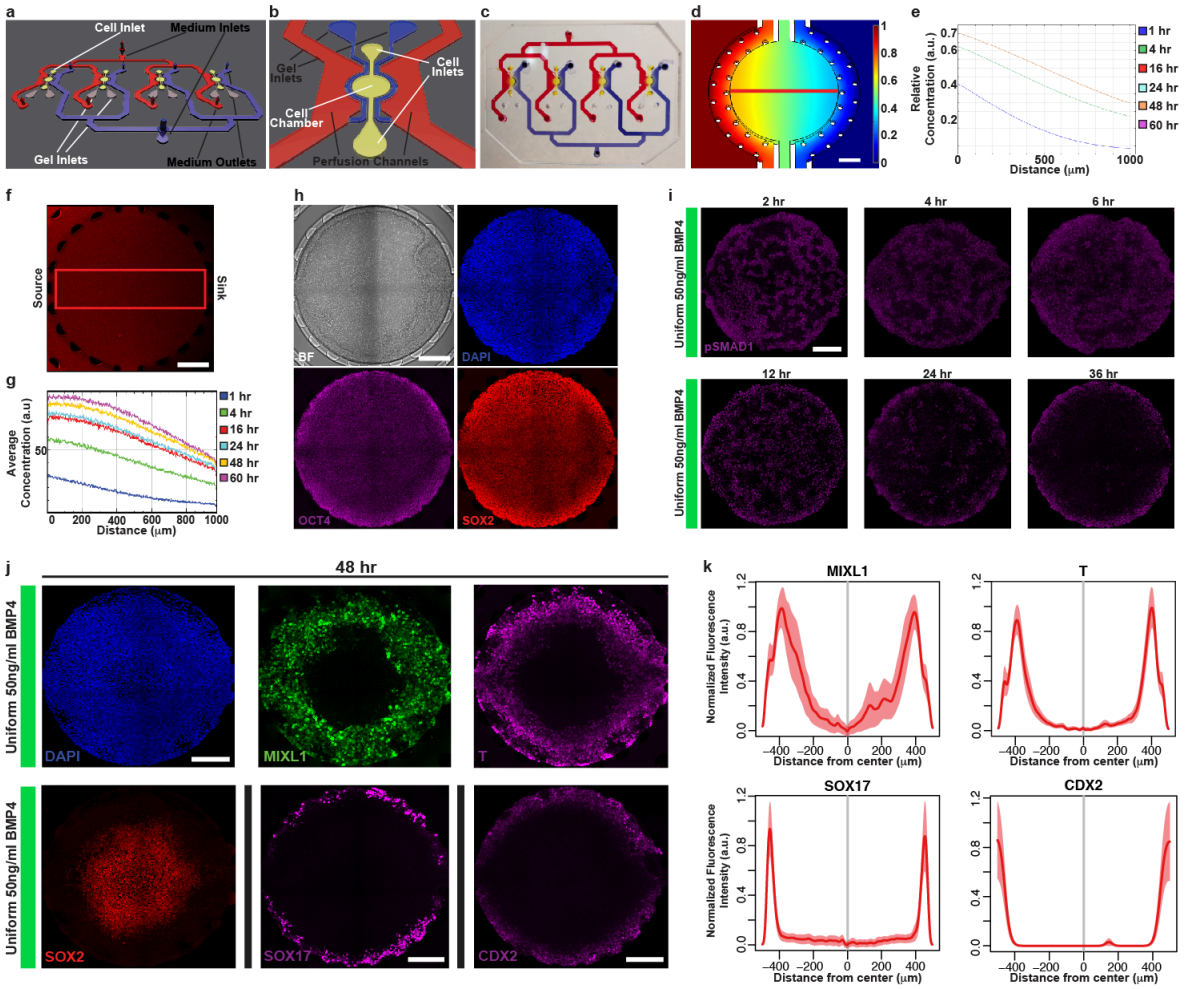

Figure 1 | **Design and characterization of the microfluidic device.** (**a**) Schematic representation of the microfluidic device. (**b**) Schematic representation of a single unit of the device. (**c**) Picture of the PDMS microfluidic device filled with colored ink in the distinct compartments. (**d**) Computational simulation of the diffusion of a reference molecule from the source side of the cell chamber after 48 hours of perfusion. (**e**) Calculated distribution of the reference molecule along the red line in **Fig. 1d** at different time points. Of note, the graphs for the later time points (16, 24, 48 and 60 hours) are overlapping. (**f**) Fluorescence picture of the cell chamber of a device perfused for 48 hours with medium containing TexasRed-labelled 40kDa-Dextran at the source and medium only at the sink. Eight samples from two independent experiments showed similar results. (**g**) Quantification of the distribution of TexasRed-labelled 40kDa-Dextran in the cell chamber at different time points. (**h**) Bright-field (BF) and fluorescence pictures of indicated markers for HES3 MIXL1$^{GFP/+}$ cultured for 96 hours under mTeSR1 medium in the microfluidic device. Eight samples from two independent experiments showed similar results. (**i**) pSMAD1 staining of HES3 MIXL1$^{GFP/+}$ cells at different time-points from the beginning of the constant and uniform exposure to 50ng/ml BMP4 mTeSR1 in the microfluidic device. Two independent experiments (each with 4 samples per time point) showed similar results. (**j**) Fluorescence pictures of indicated markers for HES3 MIXL1$^{GFP/+}$ cells after 48 hours of constant and uniform exposure to 50ng/ml BMP4 mTeSR1 in the microfluidic device. Black vertical lines separate different samples. Two independent experiments showed similar results. (**k**) Mean (line) and standard error of the mean (light-colored area) of normalized fluorescence intensity for the indicated markers along the source-sink axis of multiple cell chambers for HES3 MIXL1$^{GFP/+}$ cells exposed for 48 hours to constant and uniform 50ng/ml BMP4 (n=8 independent samples). Scale bar 200μm.

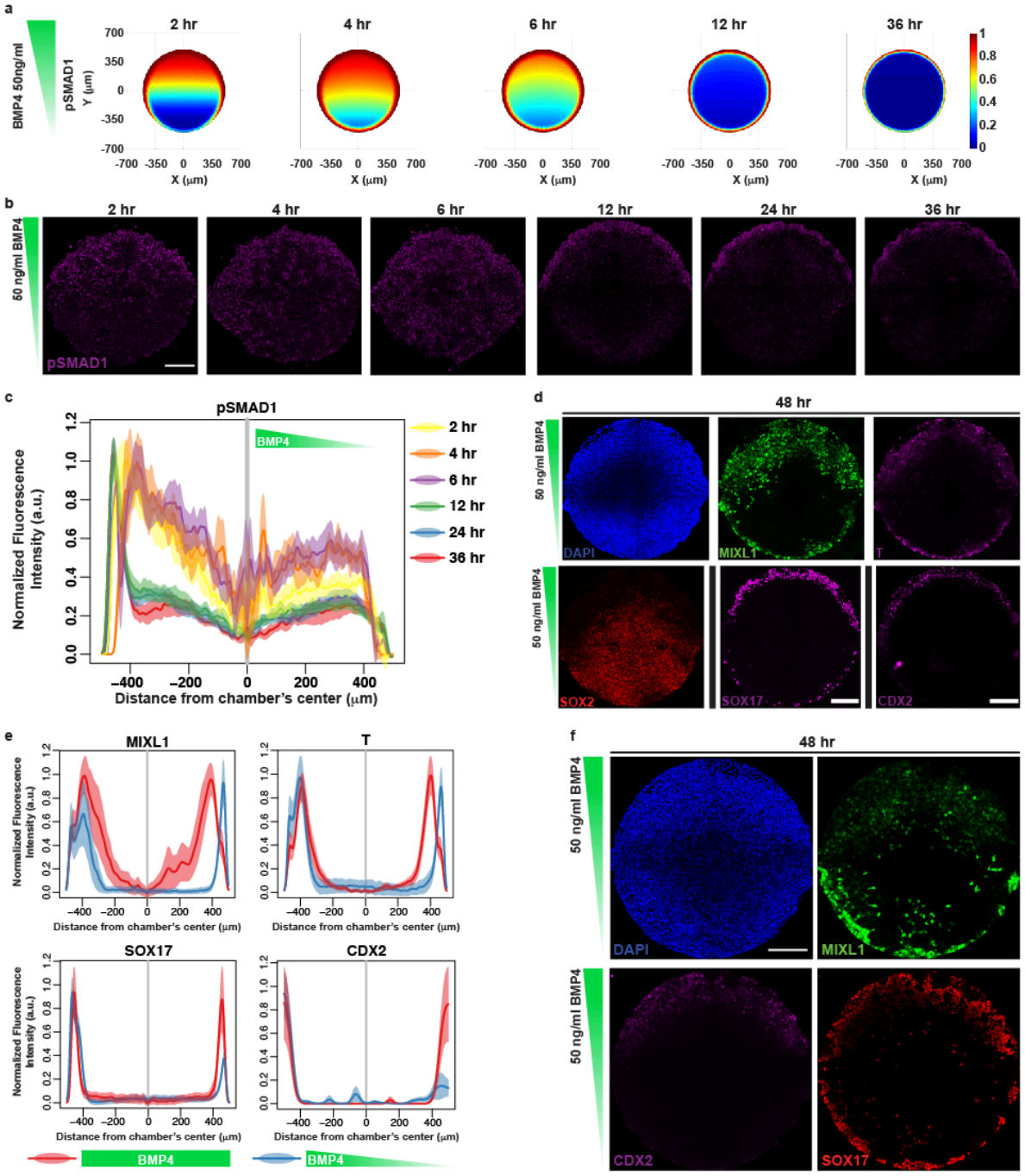

Figure 2 | A localized source of BMP4 biases the positioning of hPSC-derived germ layers. (**a**) Computational simulation showing the local percentage of pSMAD1 positive cells in a colony under the diffusion of BMP4 from a localized 50 ng/ml source. (**b**) pSMAD1 staining of HES3 MIXL1$^{GFP/+}$ cells at different time points from the beginning of the exposure to a 50ng/ml localized source of BMP4 in the microfluidic device. Two independent experiments (each with at least 4 samples per time point) showed similar results. (**c**) Mean (line) and standard error of the mean (light-colored area) of normalized fluorescence intensity for pSMAD1 along the source-sink axis of multiple cell chambers at different time points from the beginning of the exposure to a 50ng/ml localized source of BMP4 (2hr: n=7; 4hr, 36hr: n=5; 6hr, 24hr: n=6; 12hr: n=8; independent samples). (**d**) Fluorescence pictures of indicated markers for HES3 MIXL1$^{GFP/+}$ cells after 48 hours of exposure to a 50ng/ml localized source of BMP4 in the microfluidic device. Black vertical lines separate different samples. The experiment was repeated independently four times with similar results. (**e**) Mean (line) and standard error of the mean (light-colored area) of normalized fluorescence intensity for the indicated markers along the source-sink axis of multiple cell chambers after 48 hours of exposure to constant and uniform 50ng/ml BMP4 (red, n=8 independent samples) or to a 50ng/ml localized source of BMP4 (blue, n=8 independent samples). (**f**) Representative fluorescence pictures for *MIXL1*, *SOX17* and *CDX2* in HES3 MIXL1$^{GFP/+}$ cells after 48 hours of exposure to a 50ng/ml localized source of BMP4 in the microfluidic device. Similar results were observed for twelve samples from two independent experiments. Scale bar 200μm.

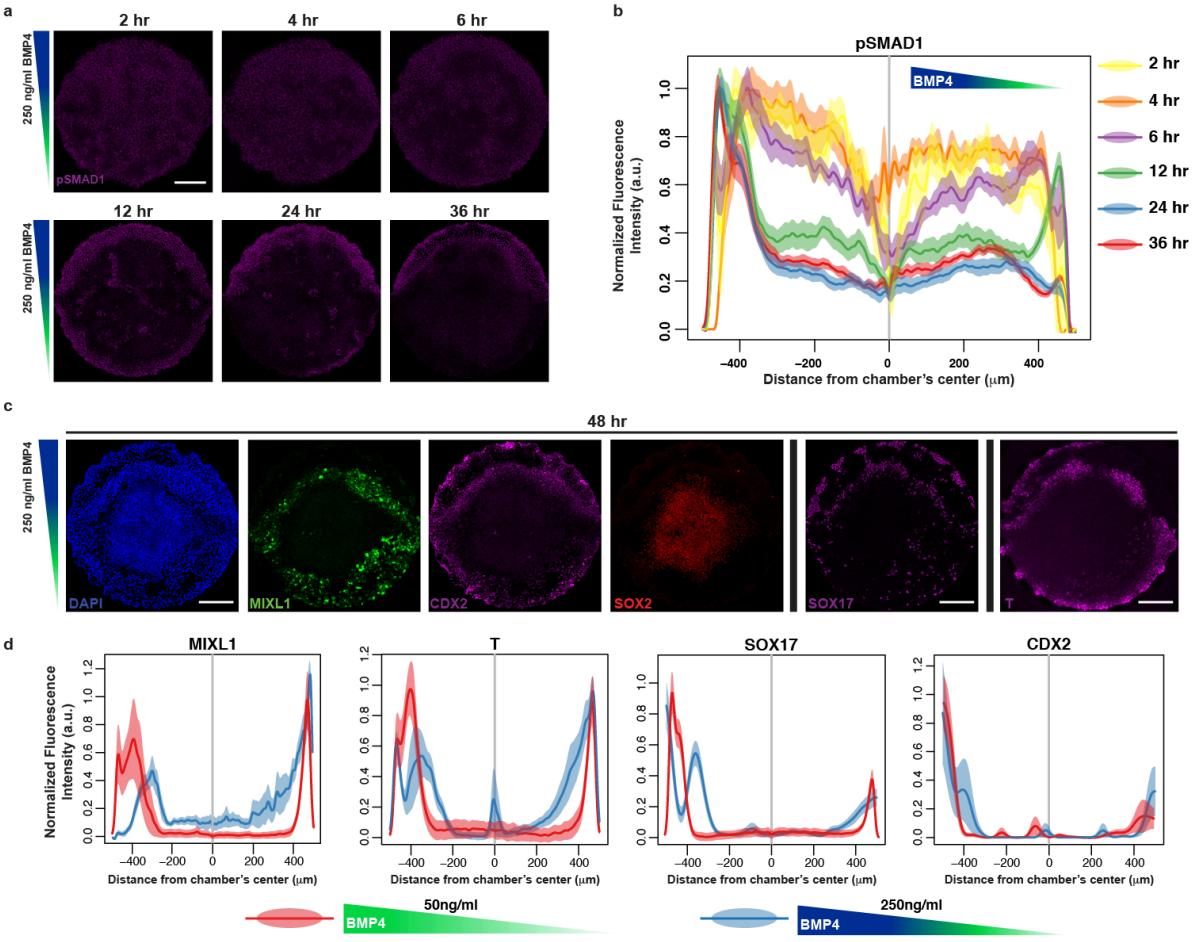

Figure 3 | **Effects of the BMP4 source concentration on hPSC patterning.** (**a**) pSMAD1 staining of HES3 MIXL1$^{GFP/+}$ cells at different time points from the beginning of the exposure to a 250ng/ml localized source of BMP4 in the microfluidic device. Two independent experiments (each with at least 4 samples per time point) showed similar results. (**b**) Mean (line) and standard error of the mean (light-colored area) of normalized fluorescence intensity for pSMAD1 along the source-sink axis of multiple cell chambers at different time points from the beginning of the exposure to a 250ng/ml localized source of BMP4 (2hr: n=5; 4hr, 6hr, 24hr, 36hr: n=7; 12hr: n=8; independent samples). (**c**) Fluorescence pictures of indicated markers for HES3 MIXL1$^{GFP/+}$ cells after 48 hours of exposure to a 250ng/ml localized source of BMP4 in the microfluidic device. Black vertical lines separate different samples. The experiment was repeated independently three times and showed similar results. (**d**) Mean (line) and standard error of the mean (light-colored area) of normalized fluorescence intensity for the indicated markers along the source-sink axis of multiple cell chambers after 48 hours of exposure to a 50ng/ml (red, n=8 independent samples) or to a 250ng/ml localized source of BMP4 (blue, n=8 independent samples). Scale bar 200μm.

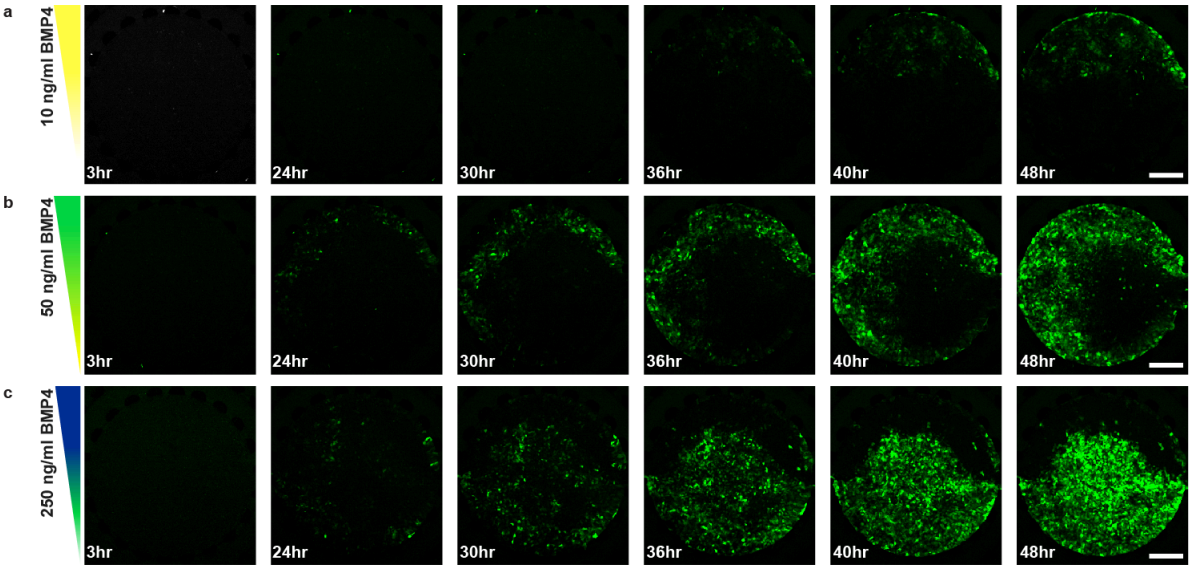

Figure 4 | **Effects of the BMP4 source concentration on hPSC patterning dynamics.** (**a**, **b**, **c)** Selected time points of time-lapse experiments on MIXL1 expression in HES3 MIXL1$^{GFP/+}$ cells. (**a**) Cells exposed to 10ng/ml localized source of BMP4. (**b**) Cells exposed to 50ng/ml localized source of BMP4. (**c**) Cells exposed to 250ng/ml localized source of BMP4. These experiments were performed on eight samples from two independent experiments per condition. For (**a**) and (**b**) the behavior were comparable to the ones reported. The condition reported in (**c**) showed a more variable phenotype with some of the samples in the two repetitions showing *MIXL1* expression extending at the colony center. Scale bar 200μm.

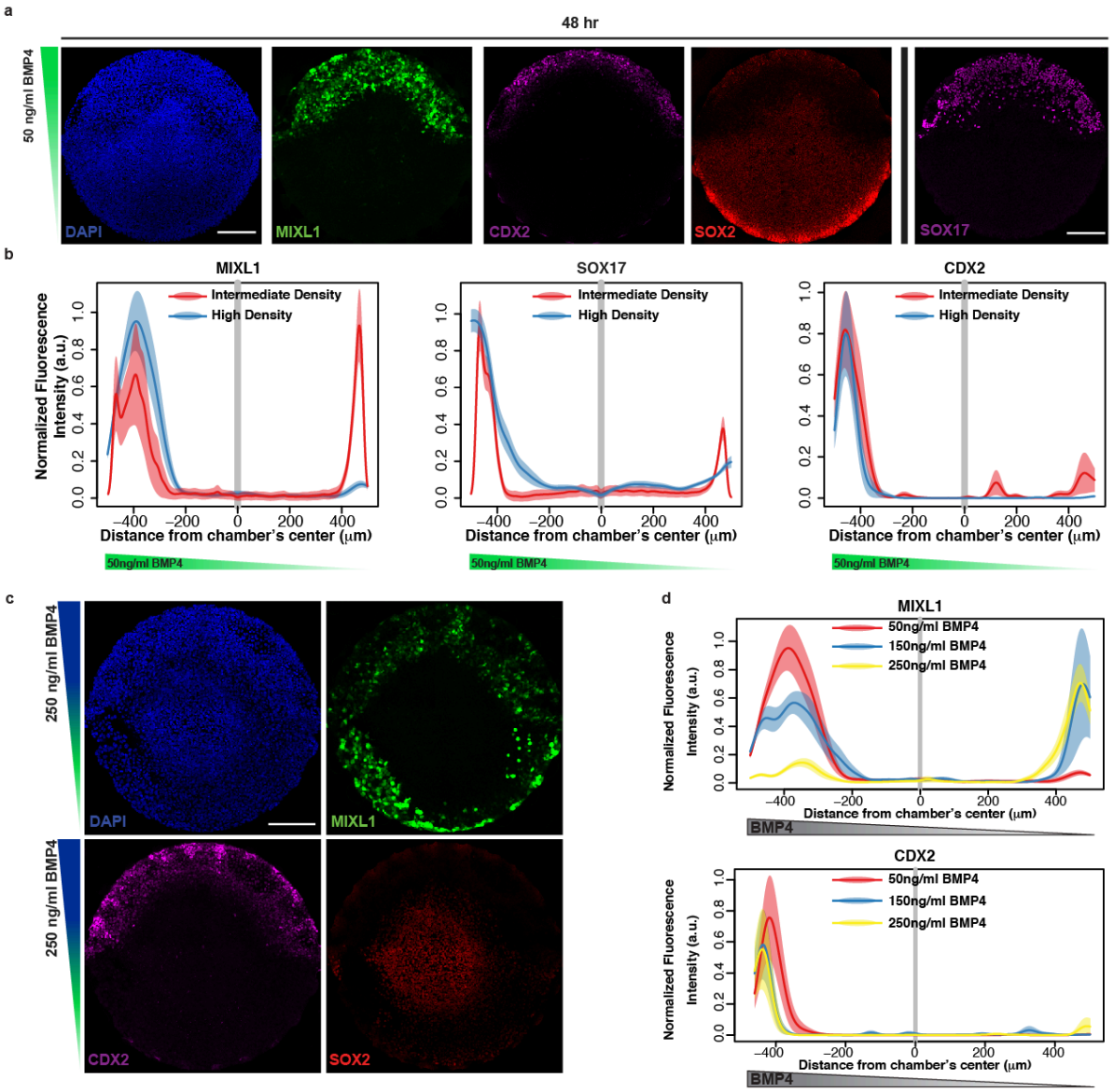

Figure 5 | The balance between cell density and BMP4 source concentration is relevant for the patterning outcome. (**a**) Fluorescence pictures of indicated markers for HES3 MIXL1$^{GFP/+}$ cells loaded at high density after 48 hours of exposure to a 50ng/ml localized source of BMP4 in the microfluidic device. Black vertical lines separate different samples. The experiment was repeated independently three times and showed similar results. (**b**) Mean (line) and standard error of the mean (light-colored area) of normalized fluorescence intensity for the indicated markers along the source-sink axis of multiple cell chambers after 48 hours of exposure to a localized 50ng/ml BMP4 source with an initial intermediate density (red, n=8 independent samples) or an initial high density (blue, n=8 independent samples). (**c**) Fluorescence pictures of indicated markers for HES3 MIXL1$^{GFP/+}$ cells loaded at high density after 48 hours of exposure to a 250ng/ml localized source of BMP4 in the microfluidic device. (**d**) Mean (line) and standard error of the mean (light-colored area) of normalized fluorescence intensity for the indicated markers along the source-sink axis of multiple cell chambers loaded at high density after 48 hours of exposure to a 50ng/ml (red, n=8 independent samples), 150ng/ml (blue, n=6 independent samples) or 250ng/ml localized source of BMP4 (green, n=6 independent samples). The experiment was repeated independently two times and showed similar results. Scale bar 200μm.

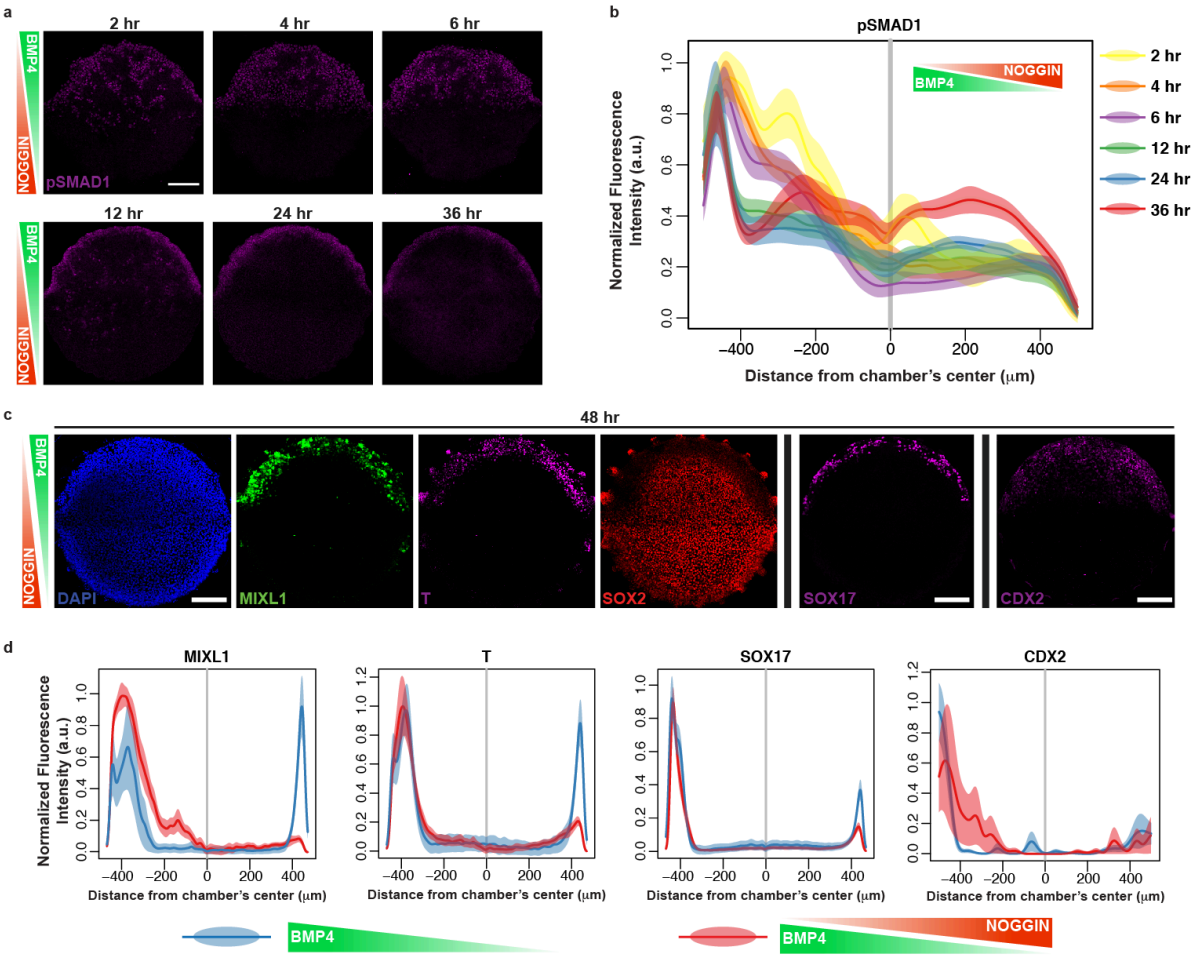

Figure 6 | Counteracting sources of BMP4 and of its inhibitor (NOGGIN) reinforce the spatial control on hPSC patterning. (**a**) pSMAD1 staining of HES3 MIXL1$^{GFP/+}$ cells at different time points from the beginning of the exposure to counteracting localized sources of 50ng/ml BMP4 and 200ng/ml NOGGIN in the microfluidic device. Two independent experiments (each with at least 4 samples per time point) showed similar results. (**b**) Mean (line) and standard error of the mean (light-colored area) of normalized fluorescence intensity for pSMAD1 along the source-sink axis of multiple cell chambers at different time points from the beginning of the exposure to localized sources of 50ng/ml BMP4 and 200ng/ml NOGGIN (2hr, 24hr: n=6; 4hr, 6hr, 12hr: n=7; 36hr: n=5; independent samples). (**c**) Fluorescence pictures of indicated markers for HES3 MIXL1$^{GFP/+}$ cells loaded at high density after 48 hours of exposure to counteracting localized sources of 50ng/ml BMP4 and 200ng/ml NOGGIN in the microfluidic device. Black vertical lines separate different samples. The experiment was repeated independently three times and showed similar results. (**d**) Mean (line) and standard error of the mean (light-colored area) of normalized fluorescence intensity for the indicated markers along the source-sink axis of multiple cell chambers after 48 hours of exposure to a localized 50ng/ml BMP4 source (blue, n=8 independent samples) or to counteracting localized sources of 50ng/ml BMP4 and 200ng/ml NOGGIN (red, n=8 independent samples). Scale bar 200μm.

Methods

Design of the microfluidic device

Some details of the device's design are reported in **Supplementary Figure 1a**. The .cif layout file containing the full design of the device (1000μm-diameter cell chamber) can be found in the associated Supplementary Material. The .cif file can be used for the fabrication of the chrome masks required for the SU8 photolitography. The two-layered device (**Supplementary Fig. 1a**) has four identical units connected in parallel to the two inlets for the medium (**Fig. 1a**). Each unit is composed of three parts: *i)* a cell chamber, *ii)* two 100μm-wide compartments for PEG-hydrogel which are fenestrated at the bottom, *iii)* two external perfusion channels (**Fig. 1b**). Taking inspiration from previously reported work on the germ layer self-organization of hESC[5], we adopted a round-shaped 1mm-diameter wide geometry for the cell chamber of the standard device. We also fabricated devices with 0.5mm diameter cell chambers (**Supplementary Fig. 5a**) and devices that allow to alternate in time the perfusion on one side of the cell chambers with two media compositions (**Supplementary Fig. 1f**). The latter device can be used for the generation of pulsatile gradients (**Supplementary Fig. 1g,h**). Cells can be loaded into the chamber through the use of dedicated inlets (**Fig. 1b**). The two layers of the device differ only at the level of the gel compartments (**Supplementary Fig. 1a**). The 50μm-thick bottom layer presents two arrays of pillars that work as phase guiding features when casting the gel (**Supplementary Fig. 1a,b,c**). The large fenestrae between the pillars permit the diffusion of molecules through the hydrogel. In the 50μm-thick top layer the arrays of pillars are replaced by two continuous PDMS walls that increase the hydrodynamic resistance between the gel compartment and the adjacent compartments thus helping to contain the not yet polymerized hydrogel between the arrays of pillars (**Supplementary Fig. 1a,c**). Once casted in the gel compartments the PEG-hydrogel surrounds the chamber and separates it from the external channels (**Supplementary Fig. 1b,c**). The hydrogel has the role to confine the cells within the chamber and to shield them from the convective flow of the medium circulating in the perfusion channels. At the same time the PEG-hydrogel allows for the passive diffusion-based mass transfer between the two external perfusion channels. Once the PEG gel is casted for each chamber, the perfusion system is split into two parallel networks (shown in red and blue in **Fig. 1a, 1c**) that can be independently perfused with media of a desired composition. To keep the concentration of molecules in the perfusion channels constant, the medium is continuously replenished via the medium inlets (**Fig. 1a**) through a pump system. Differences in the molecular composition of the medium between the two opposing channels allow for the generation of time-evolving concentration gradients following a classical source-sink model of Fickian diffusion inside each cell chamber.

The layout of the two-layered device was drawn using Clewin software (Phoenix Software). The open source graphic software Blender (Blender Foundation) was used to draw the 3D representations of the microfluidic device (**Fig. 1a**,**b** and **Supplementary Fig. 1c,f**). The layout of each layer was printed on positive-photoresist and chrome-coated glass masks (Nanofilm) using a high-resolution laser writer (VPG200, Heidelberg). The masks were then processed in an automated developer (DV10, Süss MicroTec) to remove the exposed photoresist. The underlying chrome was then etched in a solution of perchloric acid, cerium ammonium nitrate and water. The unexposed photoresist was removed with TechniStrip P1316 (Microchemicals) and finally the masks were rinsed several times with ultra-pure water and dried.

Fabrication of the SU8 mold for the PDMS device

The SU8 mold for the device was fabricated using conventional lithography methods. A 50μm-thick layer of SU8 GM1070 (Gersteltec) was spin-coated and subsequently baked at 130°C onto a pre-dehydrated and oxygen plasma-treated (Tepla300, PVA Tepla) silicon wafer using a spin coater and a hot plate (LMS200 and HP200, Sawatec) The wafer was then exposed to UV (MA6/BA6, Süss MicroTec) through the first-layer mask. After baking it at 95°C, a second 50μm-thick layer of SU8 GM1070 was spin-coated, baked and exposed to UV through the

second-layer mask that was carefully aligned to the first layer already printed on the wafer using dedicated alignment marks. The wafer was again post-exposure baked at 95°C and left undisturbed overnight. The wafer was finally developed with propylene glycol monomethyl ether acetate (Sigma), rinsed with isopropanol and baked again at 135°C overnight. The thickness of the total SU8 layer was confirmed with a surface profilometer (Dektak XT, Bruker). The wafer was then activated through oxygen-plasma treatment and silanized with trichloro (1 H, 1 H, 2 H, 2 H-per fluorooctyl) silane (Sigma) under vacuum overnight. The SU8 mold wafer was used for PDMS (Sylgard 184, Dow Corning) replica molding. The resulting PDMS replica was cut and punched with biopsy punchers of appropriate size (Kai Medical and World Precision Instruments). As substrate for the PDMS devices we used 8 well dishes (Thermo Scientific, Nunc) with the standard plastic bottom replaced by microscope glass cover-slips (Ted Pella Inc., Cat. 260460) glued with PDMS. The devices were exposed to oxygen-plasma (PDC, Harrick) and irreversibly bonded onto the glass cover slips of the dishes. The devices were then additionally sterilized under UV and kept at 37°C in humidified environment prior to their use.

Cell culture

The import and the use of hESC lines was authorized by the Office Fédéral de la Santé Publique (OFSP) after approval by the cantonal ethical commission (CER-VD). All the experiments reported in this manuscript were performed under authorization number R-FP-S-2-0014-0000. HES3 MIXL1$^{GFP/+}$ hESC were obtained from Prof. Andrew G. Elefanty (Murdoch Children's Research Institute, Parkville Victoria, Australia). RUES2 hESC were obtained from Prof. Ali H. Brivanlou (Rockefeller University, New York, US). H1 (WA01) hESC were purchased from Wicell. HYS0103 (ATCC-HYS0103) hiPSC were originally obtained from ATCC. All hESC and hiPSC lines were routinely maintained under feeder-free commercially available mTeSR1 (Stemcell Technologies) medium on cell culture dishes coated with Matrigel hESC-qualified Matrix (Corning) diluted according to the manufacturer instructions (based on the total amount of proteins measured for the specific lot). The medium was changed every day. For routine culture the cells were passaged every 4-5 days as small clumps using Gentle Cell Dissociation Reagent for cell detachment (Stemcell Technologies, Cat. 07174) and, according to confluency, they were diluted between 1:15 and 1:30. Cells were routinely checked for the absence of mycoplasma contamination. For the perfusion experiments we used mTeSR1 with 1:100 diluted Penicillin-Streptomycin (Thermo Fisher Scientific, Cat. 15140122). Gentamicin/Amphotericin B (Gibco, Cat. 5006-40) was added at final 1:1000 dilution only for the medium in the wells (external to the devices) and only at the time of perfusion.

PEG hydrogel precursor preparation

PEG hydrogels were prepared as described elsewhere[34,35]. Briefly, 8-arm PEG vinylsulfone (20kDa PEG-VS, NOF) was conjugated with Factor XIII (FXIII)-substrate peptides via Michael type reaction in 0.3M triethanolamine (pH 8.0) at 37°C for 2 h. Glutamine-containing peptide (NQ-EQVSPL-ERCG-NH2, abbreviated as NQ) or lysine-containing peptide (AcFK-GG-GPQGIAGF-ERCG-NH2, abbreviated as AF) (custom made by GLBiochem) were used in these reactions that result respectively in PEG NQ-conjugated (NQ-PEG) and PEG AF-conjugated (AF-PEG). After dialysis (Snake Skin, MWCO 10kDa, Pierce) and lyophilization, NQ-PEG and AF-PEG powders were suspended in a molar-equivalent ratio in tris-buffered saline solution (TBS, 50 mM Tris, 10 mM $CaCl_2$, pH 7.6) to form precursor solutions of AF-PEG + NQ-PEG hydrogels. To activate FXIII, 200 units/mL of fibrogammin P1250 (CSL Behring) were mixed with 20 units/mL of thrombin (Sigma-Aldrich) in the presence of 2.5 mM $CaCl_2$ at 37°C for 30 minutes.

Casting and polymerization of PEG hydrogel in the PDMS device

Before casting the PEG inside the device, the outlets of the external channels were filled with 1μl of PEG Buffer (TBS, 50mM TRIS, 10mM $CaCl_2$, 100mM NaCl, pH 7.9), avoiding to touch the phase guiding features. Activated-FXIII (FXIIIa) was mixed at 20U/ml with a 2.5% (m/v)

solution of PEG precursors in PEG Buffer. The resulting mix was carefully injected through the PEG inlets. Around 2μl were used per single gel compartment. The PEG was left to polymerize for 5 minutes at room-temperature and PEG Buffer was then loaded in the external channels, to avoid the PEG hydrogel to dry. After 15 minutes the PEG Buffer was replaced with sterile MilliQ water.

Coating of the device and cell loading

Pre-coating and coating of the cell chambers of the device were performed the day before the cell loading. The cell chamber of each unit was filled with 5μl of 0.2mg/ml Poly-D-Lysine (PDL) solution (Millipore, A-003-E) and left at room temperature for 2 hours for pre-coating. The PDMS devices were then submerged with sterile water and the PDL solution was washed aspirating twice 5ul of water through the cell chambers. The plate with the devices was left on ice for 10 minutes to cool down. From this point on, the plate with the PDMS devices was kept always on ice and/or at 4°C until cell plating. The water was removed from the wells of the plate and 5 μl of an ice-cold solution of 1:100 Matrigel (Corning, Cat. 354277) in DMEM/F12 (Thermo Fisher Scientific, Cat. 31331-028) were injected twice in each cell chamber. The devices were left at 4°C overnight for coating. The Matrigel solution was then washed by submerging the devices in PBS (Thermo Fisher Scientific, Cat. 10010-015) and aspirating 5μl of PBS inside the cell chambers. The devices were finally submerged in DMEM/F12, and 5μl were aspirated twice through the cell chambers and the external channels in the final wash step.

For cell loading we started from a culture of hESC at a confluency of 75-90%. The cells were washed with PBS and detached using TrypLE Select Enzyme (Thermo Fisher Scientific, Cat. 12563-029) by incubating them at 37°C for 5-6 minutes. The cell aggregate suspension obtained was pipetted up and down several times in the same TrypLE Select using a 1000μl pipette tip to obtain a uniform single cells suspension. The cell suspension was then transferred in a 15ml-tube containing mTeSR1 medium (1ml of TrypLE Select was mixed with 1.5 ml of mTeSR1). The suspension was mixed twice, strained through a 40μm Nylon Cell Strainer (Falcon, Cat. 352340) and the cells were spun at 140xg for 3 minutes. After the removal of the supernatant, the cell pellet was resuspended in 1ml of mTeSR1 containing 20μM Y-27632 Rock Inhibitor (Selleckchem, Cat. S1049). The cells were spun a second time at 140xg for 3 minutes. The supernatant was then removed and the cell pellet was finally resuspended in a small volume (5 wells of a 6-well plate were generally resuspended in 150 μl) of 20μM Y-27632 mTeSR1, counted using a Neubauer chamber and diluted to obtain a $30x10^6$ cells/ml suspension for the standard cell density condition or other concentrations for different cell densities. Only at this point the DMEM/F12 was removed from the dish with the PDMS devices and the dish was removed from the ice. The medium on the surface of the devices was removed as much as possible and 2.5μl of cell suspension were loaded in the cell chambers through one of the cell inlets. After 5 minutes, a second loading with 1.5 μl of cell suspension was performed per cell chamber. After 2 minutes the PDMS devices were submerged in 10μM Y-27632 mTeSR1 medium and 10μl were aspirated twice inside each external channel through the outlets. The dish with the devices was left in a cell culture incubator at 37°C for ~12 hours. The medium in the dish was then replaced with mTeSR1 medium (without Rock Inhibitor) and the unattached cells were washed out from the cell chambers by aspirating 5μl from each of the cell inlets. Occasionally some chambers showed a very low cell confluency or local aggregates of cells and they were thus not considered for the final analysis of the phenotype. After 18 hours, the cell chamber inlets of each unit were closed plugging 10μl-tips containing 10μl of mTeSR1 and the perfusion of the PDMS devices was started.

Perfusion of the PDMS devices

The perfusion of the device was performed using 0.51mm Inner Diameter Tygon Tubes (Thermo Fisher Scientific), in conjunction with Precision Tips 23GA.013X.25 (Nordson EFD) for the connection to syringes. For the connection to the inlets of the PDMS devices we used

the metal part of the Precision Tips listed above. The perfusion tubes were assembled, autoclaved and washed. The required signaling proteins were added to mTeSR1 and the medium was partially de-gassed by placing not more than 10ml per 50ml-tube in a desiccator at -800mbar and at 37°C for 2 hours. This procedure drastically reduces the formation of air bubbles in the PDMS device once the perfusion at 37°C has started. The medium was loaded in 5ml or 3ml Omnifix Luer syringes (B. Braun, 4616025V or 4616057V) according to the total volume required for the experiment. An NE-1200 Twelve Channels syringe pump (SyringePumps.com) was used for perfusion. The syringe pump was set to operate in cycles of perfusion at 3μl/min for 20 seconds and pause for 40 seconds (in total 1μl/min per device inlet corresponding to 250nl/min per single channel of each unit).

Immunofluorescence

The immunofluorescence procedure was performed on the cells directly inside the PDMS devices. For all the steps listed below, except for the incubation with primary and secondary antibodies, the devices were submerged with the step-specific solution and every time 5μl of the solution were aspirated from each channel's outlet and inlet and from each cell chamber's inlet to ensure a homogeneous distribution of the reagents. The medium was removed from each well and each compartment of the devices was washed with PBS. Fixation was performed using 4%PFA/PBS for 20 minutes at room temperature. For permeabilization we used 0.3% Triton X-100/PBS for 20 minutes at room temperature.

To block non-specific antibody binding we used 1%BSA in 0.1% Triton X-100/PBS (1% BSA PBSt) for 1 hour at room temperature. After blocking, the solution was removed from the wells and 5μl of the primary antibodies solution were injected through each cell chamber inlet and each perfusion channel inlet and outlet of the devices. The incubation with primary antibodies was performed in 0.5% BSA PBSt for 48 hours at 4°C. To avoid the solution to dry, the devices were covered with a piece of Parafilm (Sigma, BR701605-12EA). According to the specific primary antibody a refill of antibody solution could be performed after 24 hours of incubation. Washing with PBSt for 30 minutes was repeated three times. Incubation with secondary antibodies and DAPI was performed as described for the primary antibodies for 48 hours at 4°C in the dark. Wash with PBSt was performed as described above for the primary antibodies. The devices were rinsed with PBS and they were kept submerged with PBS in each well of the plate. They were visualized immediately after this procedure. For long-term storage, PBS was removed from the wells and 5 μl of Vectashield Mounting Medium for Fluorescence (Vector Laboratories, Cat. H-1000) were injected in the cell chambers and in the channels and the plate was stored at 4°C in the dark.

For phospho-Smad1/5 Ser463/465 (pSMAD1) staining, the permeabilization was performed in 1%SDS PBS at 37°C for 30 minutes. Moreover, Phosphatase Inhibitor Cocktail 3 (Sigma, P0044) was added at a 1:100 dilution to permeabilization, blocking, primary and secondary antibodies incubation solutions.

The primary antibodies and the related dilutions used were: anti-Brachyury/T 1:300 (R&D Systems, AF2085), anti-Sox2 1:500 (Abcam, ab97959), anti-Oct4 1:500 (Santacruz, sc-5279), anti-Sox17 1:100 (R&D Systems, AF1924), anti-CDX2 1:100 (Abcam, ab15258 or Novus Biologicals, NB100-699), anti-pSMAD1 1:100 (CST, 9516). The secondary antibodies used and their respective dilution were: donkey anti-rabbit Alexa 568 1:200 (Thermo Fisher Scientific, A10042), donkey anti-rabbit 647 1:200 (Thermo Fisher Scientific, A31573), donkey anti-goat Alexa 633 1:200 (Thermo Fisher Scientific, A21082), donkey anti-goat Alexa 568 1:200 (Thermo Fisher Scientific, A11057), donkey anti-goat Alexa 488 1:200 (Thermo Fisher Scientific, A11055), donkey anti-mouse Alexa 647 1:200 (Thermo Fisher Scientific, A31571). For pan-nuclear staining we used DAPI (Thermo Fisher Scientific, D1306) at 1:1000 dilution.

Imaging of biological samples and image processing

Pictures of fixed cell samples were acquired with an inverted laser-scanning confocal microscope (Zeiss, LSM700). The signal for each fluorophore was acquired in a dedicated

acquisition step. In each experiment a negative control for the primary antibodies was used as a reference for the secondary antibodies and general background. Samples for quantitative analysis were imaged using a 10X-magnification objective. Representative pictures were additionally acquired with a 20X-magnifictaion objective. In the case of 20X-magnification to visualize the whole chamber we acquired four partially overlapping fields (15% overlap) and then stitched them using the Grid/Collection Stitching plugin of Fiji/ImageJ[36]. At least 4 stacks were taken covering the thickness of each sample. The stacks were then Z-projected with Fiji/ImageJ using the maximum intensity values. For time-lapse experiments with living cells we used a spinning-disc confocal microscope (Olympus IX83 equipped with a Yokogawa CSU-W1 module or Nikon Eclipse TI equipped with spinning disc confocal module) with a 10X-magnification objective. In cases of representative pictures (used for visualization purposes only) where the signal was too low to appreciate (pSMAD1 and CDX2), we enhanced the contrast of the signal equally across the whole image. We took care that the contrast enhancement did not affect the essence of the results and we used as a reference the negative controls acquired in the same experiments to discern the specific signal from the background.

Determination of initial cell density in the cell chamber

Cell suspensions at different concentration were loaded, as previously described, in the cell chambers: "Low density" ($15*10^6$ cells/ml), "Intermediate density" ($30*10^6$ cells/ml) or "High density" ($60*10^6$ cells/ml). Cells were left in 10μM Y-27632 mTeSR1 medium in the incubator for 12 hours. The medium was then changed to mTeSR1 only medium and the chambers were washed by aspirating 5μl of medium through each of the cell inlets. The device was left for additional 18 hours in incubator. Cells were then fixed, as described above, and their nuclei stained using DAPI. Images of 8 cell chambers per condition were acquired as described above.

For each image we counted the number of nuclei contained in 3 not overlapping squares of 200x200μm (area per square: 40000 μm^2) and we calculated their average to account for eventual local differences in cell density. The boxplots of **Supplementary Fig. 7c** show the distribution of these averages for each of the three density condition. Single data points are reported in red. An ANOVA test and a subsequent multiple t-test (two-sided, with p-value Benjamini-Hochberg corrected for multiple testing) have been performed and resulted in statistically significant differences in cell number among the three density conditions (for the ANOVA test $F(2,22)= 132.6$, $p(>F)= 8.75*10^{-11}$; for the t-tests the p-values are reported in **Supplementary Fig. 7c**).

Image analysis

We performed the immunofluorescence image analysis of our chambers using R version 3.2.2 and the EBImage package[37]. For the fluorescence intensity based analysis, we first detect the chamber inside every image by using the DAPI signal. This is done by first smoothing the image by averaging pixel contained inside a disc of 15 pixels of diameter. After using the Otsu's threshold to segment the chamber from the background, filling up holes and keeping the largest object in the image we obtained a region corresponding to the inside of the chamber. We then use the circle that encompasses this region as our chamber. All the chamber profiles are then computed from this region. We subdivided the chamber in two regions, a first one representing the top-half of the chamber (close to one of the perfusion channel) and a second representing the bottom-half of the chamber (close to the opposite perfusion chamber). We compute the average signal within one region of the chamber by averaging the signal that goes from the center to the border of the chamber. Briefly, this is done by drawing multiple virtual lines running from the center to the border of the chamber and keeping track of pixel intensities along these virtual lines. We average the profiles of lines drawn at every angle from 0 to π with a 0.05 radians step. We performed this analysis for *MIXL1*, *T*, *SOX17, CDX2* and pSMAD1 immunofluorescences separately on the two regions

of each chamber for each distinct sample. Finally, we smooth the signal using a lowess function before performing a quantile normalization by subtracting the 1st percentile and divide by the 99th percentile values. In this way, all the signal for each image is normalized between 0 and 1. The reported graphs (**Fig. 1k, 2c, 2e, 3b, 3d, 5b, 5d, 6b, 6d** and **Supplementary Fig. 4c, 4e, 5e, 9c, 9e, 10b**), represent the average of all the images (with the standard error of the mean) for each condition.

To calculate the percentage of marker-positive cells we restricted our analysis to a rectangular area of 195μm x 1000μm, extending from source to sink and centered at the center of the chamber. Inside this area, nuclei were manually identified and their positions extracted using a dedicated Fiji/ImageJ tool. For each marker, background corrected images for each condition were used to determine which of the previously identified nuclear positions were positive for each specific marker. We then subdivided the area of analysis for each image in 21 subsections (bins) each with a width of ~47.5μm, going from the source (bin 1) to the sink (bin 21) and calculated the percentage of nuclei positive for a specific marker in each bin for each distinct sample. The boxplots of **Supplementary Fig. 3b, 6a, 7d, 7e, 8a** show the percentage of marker-positive cells for all the images of a specific experimental condition. Each graph represents the spatial distribution of marker-positive cells along the source-sink axis of the chamber. In the boxplots the center line represents the median, the box limits represent the first and third quartiles, the whiskers represent the upper and lower extremes of the distribution, while white circles represent outliers (defined as a data point located more than 1.5 times outside the interquartile range above the upper quartile or below the lower quartile). Single data points are shown in red.

Computational simulation of concentration gradients dynamics

The modeling software COMSOL Multiphysics (COMSOL AB) was used to perform the simulation of the diffusion of soluble molecules within the device. We chose to model the diffusion of 40kDa Dextran molecules, being the molecular weight of these comparable to that of many cell-secreted signaling proteins and being Dextran readily available in fluorescently labeled form usable for experimental validation of the simulated behavior. The simulation model was reasonably simplified while key dimensions and physical entities were respected. The diffusion coefficient of the dextran molecule with molecular weight of 40kDa in water ($D_w = 4.4 \times 10^{-7}$ cm^2/s) was based on previously reported measurements[38]. The diffusion coefficient in the PEG hydrogel ($D_g = 2.2 \times 10^{-7}$ cm^2/s) was experimentally obtained as previously described[39]. Because of the continuous perfusion at high flow rate (0.25μl/min per perfusion channel of single unit), the concentration within the source and sink has been assumed constant and was set at 1 and 0, respectively. Simulative quantification of the molecule's distribution in the device was performed for a duration of 60 hours at 10 minutes intervals to evaluate both the dynamics and stability of the system. The graphs of **Fig 1e** represent the concentration profile along a segment spanning along the whole 1mm-diameter chamber (from source to sink) intersecting the center of the chamber and located at 50μm from the bottom of the device, as shown in **Fig. 1d**. The gradient is rapidly established, evolves over time and stabilizes after approximately 16 hours with a concentration difference between the source and sink of approximately 2.5-fold at equilibrium. The graphs of **Supplementary Fig. 1d,e** show the concentration profiles on the curved blue segments that extend along the edges of the chamber as reported in the figures. The graphs of **Supplementary Fig. 5c** represent the concentration profile along a segment spanning the whole 0.5mm-diameter chamber (from source to sink) intersecting the center of the chamber and located at 50μm from the bottom of the device, as shown in **Supplementary Fig. 5b**.

Experimental characterization of concentration gradients in the PDMS device

Time-lapse experiment was performed on an inverted laser-scanning confocal microscope (Zeiss, LSM700). The devices, in this case composed of a single unit, were perfused with medium containing 33μg/ml 40kDa-Dextran TexasRed-Labeled (Thermo Fisher Scientific, Cat. D1829) on one side of the chambers and with medium only on the other side. The

acquisition was performed with a 10X-magnification objective. 40kDa-Dextran TexasRed-Labeled was chosen according to the fact that its molecular weight is comparable to that of many cell-secreted signaling proteins. To set the background for the TexasRed signal we referenced to a device perfused only with medium. The signal of each time-point was then analyzed with the Plot Profile function of Fiji/ImageJ, which averages the signal inside a rectangular selection spanning the whole length of the chamber (**Fig. 1f,g and Supplementary Fig. 1g,h**).

Computational simulation of phospho-SMAD1 patterning

The impact of BMP4 sources on the pSMAD1 profile was predicted computationally by adapting the edge sensing and inhibitor model presented by Etoc et al, 2016[14]. To cope with the 2D geometry of our device and the externally applied gradients, the original model was transformed from radial to Cartesian coordinates. Briefly, pSMAD1 response was modeled identically as in the original model (reproduced here for clarity, see Eq. 1) using a Hill function with coefficient n=1.4, and an inflexion point $K_{mp}(r,N_{cell})$ that depends on cell density N_{cell} and radial position r.

$$(1)\ pSMAD1(r, N_{cell}) = \frac{B_f^n}{B_f^n + K_{mp}(r, N_{cell})^n}$$

In all the equations, B_f indicates the concentration of free BMP4 (not bound to NOGGIN), while B indicates the total concentration of BMP4 and N the concentration of NOGGIN. The function K_{mp}, reflecting the sensitivity of the response, was adapted from the original paper[14]. To model colonies with larger radii of 500µm instead of 250µm, the low sensitivity central region was extended while keeping the same higher BMP4 sensitive region at the colony edge. It was indeed reported that patterning at the edge of the colony does not vary when colony size is changed[5]. Since BMP4 is antagonized by the binding with NOGGIN (N), the free BMP4 (B_f) available for signaling was modeled as follows (Eq. 2):

$$(2)\ B_f = B\left(\frac{1}{1+aN}\right)$$

Diffusion of NOGGIN and BMP4 was modeled in 2D using Fick's law (Eq. 3 and 4) with respective diffusion constants D_N = 10µm^2/s and D_B = 10µm^2/s. Degradation rates λ_N and λ_B have been set to zero, as these values have been previously shown to provide a good approximation to the real data[14].

$$(3)\ \frac{\partial N}{\partial t} = D_N\left(\frac{\partial^2 N}{\partial x^2} + \frac{\partial^2 N}{\partial y^2}\right) - \lambda_N N + p(x, y, t)$$

$$(4)\ \frac{\partial B}{\partial t} = D_B\left(\frac{\partial^2 B}{\partial x^2} + \frac{\partial^2 B}{\partial y^2}\right) - \lambda_B B$$

To take into account the geometry of our device, the modeled spatial domain was defined as a rectangle of size 1400µm x 2200µm (height x width), and the cell colony defined as a circle of radius 500µm centered on the center of the domain (**Fig. 2a, Supplementary Fig. 2g, 3a, 7a,f**). The 200µm above and below the colony were added as the source and sink channels of the device are located at such boundaries. A constant concentration Dirichlet boundary condition was applied at these locations as we can assume that the perfusion in the channels is sufficient to provide a constant concentration. On the other hand, a no flux Neumann boundary condition was applied at the left and right domain boundaries. These boundaries were placed at 600µm as this was the minimum distance that was able to replicate the circular pSMAD1 symmetry originally reported[14]. Finally, the NOGGIN production $p(x,y,t)$ was modeled proportionally to the normalized pSMAD1 profile as in the original model (reproduced in Eq. 5), the density of cells, and the interpolated single cell NOGGIN mRNA number reported originally[14].

$$(5)\quad p(x,y,t) = mRNA_{NOG}(t) * N_{cell}(t) * \frac{pSMAD1(x,y,t)}{\sum_{x^2+y^2\leq r^2} pSMAD1(x,y,t)}$$

The model was solved numerically using a custom code and the partial differential equation toolbox on MATLAB R2016b. The maximal mesh edge length was set to 15µm. The initial cell density (N_{cell}) was set to 2200 cells/mm^2 for the intermediate cell density condition (**Fig. 2a and Supplementary Fig. 2g, 3a**) and to 4400 cell/mm^2 (twice the intermediate density) for the high cell density condition (**Supplementary Fig. 7a,f**). The cell doubling time was set to 16.8h. All numerical values were chosen as proposed in the original publication or adjusted to match the pSMAD1 profile originally reported under constant BMP4 conditions[14]. Hence, for the currently proposed geometry, the optimal value of the free parameter a was set to 10.

Reporting Summary
Further information on research design is available in the Nature Research Life Sciences Reporting Summary linked to this article.

Data availability
All relevant data are available upon reasonable request from the corresponding author.

Supplementary references

34. Ehrbar, M. *et al.* Enzymatic formation of modular cell-instructive fibrin analogs for tissue engineering. *Biomaterials* **28**, 3856–3866 (2007).
35. Ehrbar, M. *et al.* Biomolecular Hydrogels Formed and Degraded via Site-Specific Enzymatic Reactions. *Biomacromolecules* **8**, 3000–3007 (2007).
36. Preibisch, S., Saalfeld, S. & Tomancak, P. Globally optimal stitching of tiled 3D microscopic image acquisitions. *Bioinformatics* **25**, 1463–1465 (2009).
37. Pau, G., Fuchs, F., Sklyar, O., Boutros, M. & Huber, W. EBImage--an R package for image processing with applications to cellular phenotypes. *Bioinformatics* **26**, 979–981 (2010).
38. Arrio-Dupont, M., Cribier, S., Foucault, G., Devaux, P. F. & d'Albis, A. Diffusion of Fluorescently Labeled Macromolecules in Cultured Muscle Cells. *Biophys. J.* **70**, 2327–2332 (1996).
39. Brandenberg, N. & Lutolf, M. P. In Situ Patterning of Microfluidic Networks in 3D Cell-Laden Hydrogels. *Adv. Mater.* **28**, 7450–7456 (2016).